THE ASTROPHYSICAL JOURNAL, 397:187–195, 1992 September 20

AN AXISYMMETRIC MAGNETOHYDRODYNAMIC MODEL FOR THE CRAB PULSAR WIND BUBBLE

MITCHELL C. BEGELMAN[1] AND ZHI-YUN LI
Joint Institute for Laboratory Astrophysics, University of Colorado and National Institute of Standards and Technology, Boulder, CO 80309-0440
Received 1992 February 3; accepted 1992 March 30

ABSTRACT

We extend Kennel & Coroniti's spherical magnetohydrodynamic models for the Crab Nebula to include the pinching effect of the toroidal magnetic field. Since the bulk nebular flow is likely to be very submagnetosonic, a quasi-static treatment is possible. We show that the pinching effect can be responsible for the observed elongation of the pulsar wind bubble, as indicated by the surface brightness contours of optical synchrotron radiation. From the observed elongation we estimate a value for σ, the ratio of Poynting flux to plasma kinetic energy flux in the free pulsar wind, which is consistent with previous results from spherical models. Using the inferred magnetic field configuration inside the pulsar wind bubble, combined with the observed dimensions of the X-ray nebula, we are able to constrain the particle distribution function. We conclude that, for a power-law injection function, the maximum energy has to be much larger in the pulsar equatorial region than in the polar region. Larger minimum energy near the equator is also desirable in order to bring the computed contours into closer agreement with those observed, suggesting that the free pulsar wind moves faster near the equator than near the poles. Finally, we describe how the interaction of the magnetic field with the "bays" in the synchrotron nebula could produce the "hourglass" shape of the total polarized optical light found by Michel et al.

Subject headings: ISM: bubbles — ISM: individual (Crab Nebula) — MHD — pulsars: individual (Crab Nebula)

1. INTRODUCTION

Although the Crab Nebula is by far the best studied supernova remnant (Trimble 1985), many important issues remain unresolved. Among them is the question of how the spindown energy of the Crab pulsar is transformed into synchrotron emission inside the nebula. Rees & Gunn (1974) proposed that the spindown luminosity can be carried out from the pulsar in a wind consisting of a mixture of magnetic field, relativistic particles, and large-amplitude 30 Hz waves, but they left the energy partition between these constitutents unspecified. In order for the pulsar wind to come into pressure equilibrium with its surroundings, a strong standing MHD shock forms about 0.1 pc from the pulsar, at which most of the kinetic energy in the free pulsar wind is converted into internal energy of the shocked wind material. The Poynting flux in the free wind just upstream of the shock is required to be much smaller than the kinetic energy flux ($\approx 1\%$). Downstream of the standing shock is a large volume (compared to that of the free wind) of relativistically hot, shocked wind fluid which is called the Crab pulsar wind bubble. Most of the infrared through X-ray synchrotron radiation comes from the wind bubble, and it is the structure of this region that we shall study in the present paper. Rees & Gunn's (1974) model has been elaborated on by Kennel & Coroniti (1984a, hereafter KC1), who considered the bubble to contain a dense electron-positron plasma in which large-amplitude 30 Hz waves cannot propagate (Michel 1982; Arons 1991). They found that the value of σ, defined to be the ratio of the Poynting flux to the plasma kinetic energy flux in the free pulsar wind, must be very small ($\approx 3 \times 10^{-3}$). Evolutionary calculations carried out by Emmering & Chevalier (1987) indicated a somewhat smaller σ, of about 1.6×10^{-3}. In a paper accompanying KC1, Kennel & Coroniti (1984b, hereafter KC2) were also able to account reasonably well for the spectral and spatial distributions of the synchrotron radiation emanating from the pulsar wind bubble.

All of the models mentioned above have assumed spherical geometry, yet the optical and X-ray synchrotron nebulae are substantially elongated along orthogonal axes (Woltjer 1957; Pelling et al. 1987). The spherical models have to be modified if one is to understand these elongations and to use them to derive additional insight into the nature of the Crab Nebula. As far as we know, the axisymmetric model we present in this paper is the first quantitative effort to explain the elongation of the Crab Nebula as a consequence of its hydromagnetic structure.

The magnetic field inside the wind bubble is expected to be predominantly toroidal (Rees & Gunn 1974; KC1) as a result of winding by the pulsar's rotation, and well-ordered toroidal field around the Crab pulsar's rotation axis is consistent with optical polarization observations (Schmidt, Angel, & Beaver 1979; Arons 1991). The spherical symmetry assumed in previous MHD models should break down when the magnetic pressure is comparable to or greater than the gas pressure, since the pinching force due to the toroidal field then becomes dynamically important. The magnetic pinching effect is taken into account in our model, and is crucial in our explanation of the wind bubble's shape. As a result, the flow equations are two-dimensional and cannot readily be integrated, in contrast to the spherical flow case (KC1). In general, this would render it very difficult to solve for the hydromagnetic structure of the wind bubble. However, the bulk flow is highly submagnetosonic with respect to the magnetized relativistic fluid which is believed to fill the wind bubble, except perhaps close

[1] Also at Department of Astrophysical, Planetary and Atmospheric Sciences, University of Colorado at Boulder.

to the shock which terminates the free pulsar wind. Therefore, the plasma inertia can be neglected to lowest order and a quasi-static treatment of the fluid inside the wind bubble is possible. This treatment is given in § 2. It turns out that both the gas pressure and the magnetic field strength are approximately functions of the cylindrical radius alone, and that the interior structure can be expressed as a two-parameter family of analytic models. Remarkably, all details of the velocity field drop out of the problem.

To counterbalance the magnetic pinching force, a pressure gradient has to set up in the cylindrically radial direction and the total (gas + magnetic) pressure has to decrease monotonically away from the pulsar rotation axis (which is presumably along the NW-SE direction on the plane of the sky). We believe that this pressure difference across the wind bubble is sufficient to cause the overall nebular shape to deviate from a perfect sphere and to elongate in the same direction as the pulsar rotation axis. The elongation of the network of optical filaments in the same direction could result from coupling of the filaments to the underlying flow of the wind bubble, and thus there might be no need to invoke an intrinsically asymmetric supernova explosion. By following the time evolution of the Crab pulsar wind bubble explicitly in § 3, we show that the magnetic pinching is sufficient to account for the present-day shape of the nebula. Our estimated value for σ agrees with earlier spherical models, thus providing an independent check on the consistency of our analysis with previous treatments.

Both soft and hard X-ray nebulae are observed to be considerably smaller than the optical nebula and are elongated along the pulsar rotational equator (Aschenbach & Brinkmann 1975; Harnden & Seward 1984; Pelling et al. 1987). In § 4, we make use of the size and shapes of these X-ray nebulae, together with the magnetic field structure inferred from our pulsar wind bubble evolution calculations, to constrain the synchrotron particle distribution function. We find that, in agreement with the torus model proposed by Aschenbach & Brinkman (1975), the high-energy X-ray–emitting particles have to be concentrated in the pulsar equatorial region. We discuss our results in § 5 and describe how the interaction of the magnetic field with the "bays" in the optical synchrotron nebula (see Fesen, Martin, & Shull 1992 for a description) could lead to an "hourglass" morphology in the total polarized light, as found by Michel et al. (1991).

2. QUASI-STATIC STRUCTURE OF PULSAR WIND BUBBLE INTERIOR

2.1. *Basic Equations*

We adopt a cylindrical coordinate system, (r, φ, z), and assume that all fluid variables are independent of φ and time t. If, in addition, the flow velocity $\boldsymbol{v}$ has no φ-component, then the continuity equation $\nabla \cdot (n\boldsymbol{v}) = 0$ is satisfied identically by

$$v_r = -\frac{1}{nr}\frac{\partial \psi}{\partial z}, \quad v_z = \frac{1}{nr}\frac{\partial \psi}{\partial r}, \tag{1}$$

where ψ is the stream function, n is the number density, and v_r and v_z are the two velocity components. If we assume that the magnetic field is purely toroidal, $\boldsymbol{B} = B(r, z)\hat{\varphi}$, then the flux-freezing condition, $\nabla \times (\boldsymbol{v} \times \boldsymbol{B}) = 0$, has only a φ-component,

$$\frac{\partial (Bv_z)}{\partial z} + \frac{\partial (Bv_r)}{\partial r} = 0 . \tag{2}$$

The assumption of purely toroidal magnetic field may be invalidated if distortions of the magnetic field by the network of optical filaments (Michel et al. 1991) or the dark "bays" (Fesen et al. 1992) become important. We neglect this possibility here.

The steady state momentum equation for axisymmetric flow can be written as

$$\nabla\left(P + \frac{B^2}{8\pi}\right) + \frac{B^2}{4\pi r}\hat{e}_r = -\rho\left[\nabla \frac{v^2}{2} - \boldsymbol{v} \times (\nabla \times \boldsymbol{v})\right]. \tag{3}$$

The terms on the left-hand side are the gas and magnetic pressure forces and the magnetic pinching force, while those on the right-hand side are the plasma inertial forces.

To close the system of equations, we need an equation of state. For an isotropic, relativistically hot fluid inside the wind bubble, the gas pressure P is one-third of the internal thermal energy density e, and the sound speed equals $c/3^{1/2}$. If synchrotron losses do not reduce the gas pressure much (KC1), then the relativistically hot fluid flows adiabatically along each streamline ψ. Therefore, one can relate the gas pressure P to the number density n by

$$P = A(\psi)n^{\Gamma}, \tag{4}$$

where the adiabatic index $\Gamma = 4/3$, and the function $A(\psi)$ depends on the flow entropy along each streamline.

2.2. *Quasi-static Flow Solution*

Pressure imbalances in an axisymmetric MHD flow containing purely toroidal field are rectified by the propagation of fast magnetosonic waves, the speeds of which always exceed that of sound ($\approx c/3^{1/2}$) and approach the speed of light when the magnetic pressure is much larger than the gas pressure (KC1). Since the bulk flow speed for most parts of the wind bubble is expected to be much less than the speed of light (KC1), one can treat the flow as being in hydrostatic equilibrium, i.e.,

$$\frac{\partial}{\partial z}\left(P + \frac{B^2}{8\pi}\right) = 0 \tag{5}$$

and

$$\frac{\partial}{\partial r}\left(P + \frac{B^2}{8\pi}\right) = -\frac{B^2}{4\pi r}. \tag{6}$$

It follows immediately from equation (5) that $P + B^2/8\pi$ is independent of z. Equation (6) then implies that both P and B must be functions of cylindrical radius r alone.

Now, from the equation of state (4), we have $n = [P(r)/A(\psi)]^{1/\Gamma}$. Therefore the continuity equation, written in the form

$$\frac{\partial}{\partial r}(nrv_r) + \frac{\partial}{\partial z}(nrv_z) = 0,$$

is equivalent to the equation

$$\frac{\partial}{\partial r}(P^{1/\Gamma}rv_r) + \frac{\partial}{\partial z}(P^{1/\Gamma}rv_z) = 0 . \tag{7}$$

Comparing equation (7) with equation (2), and making use of the fact that both P and B are z-independent, we finally arrive at a relation between P and B:

$$P(r) = C_1\left[\frac{B(r)}{r}\right]^{\Gamma}, \tag{8}$$

where C_1 is an integration constant. Armed with this relation, one can now integrate equation (6) to solve for P and B. Denoting the ratio of gas pressure to magnetic pressure by β, i.e., $\beta \equiv 8\pi P/B^2$, we obtain, after some lengthy manipulations,

$$\beta[\Gamma\beta + 2(\Gamma - 1)]^{\Gamma - 2} = C_2 r^{-2(\Gamma - 1)}, \quad (9)$$

where C_2 is another constant of integration. As we shall see below, a physically more meaningful constant is the scale length $H \equiv C_2^{2(\Gamma-1)}$, so that we can define $x \equiv r/H$ and $y \equiv z/H$. Letting $\eta = 9\beta x^2/16$ and setting $\Gamma = 4/3$, we can rewrite equation (9) as

$$(\eta + \tfrac{9}{32}x^2)^{2/3} = \eta . \quad (10)$$

Finally, we have

$$P = \frac{P_0}{\eta^2}, \quad \frac{B^2}{8\pi} = \frac{9P_0 x^2}{16\eta^3}, \quad (11a, 11b)$$

where the constant $P_0 \equiv (6\pi)^2 C_1^3/H^4$ is the gas pressure on the pulsar rotation axis (i.e., $r = 0$), since $\eta = 1$ at $x = 0$.

It is worth noting that the streamline-dependent entropy function $A(\psi)$ (cf. eq. [4]) drops out of the problem (when deriving eq. [7]) in our quasi-static treatment, and the velocity field is completely decoupled from the determination of the pressure and the magnetic field structure to lowest order. To recover the velocity field, one would have to expand the momentum equation (3) to higher order. This is possible in principle, but the uncertainites in the flow boundary conditions at the wind-terminating shock, which depend on the detailed structure of the free pulsar wind, render the exercise impractical at present.

We solve equations (10) and (11) numerically, and plot the total pressure $P_{tot} = P + B^2/8\pi$ in units of P_0 against x in Figure 1. The total pressure indeed declines outward in order to counterbalance the inward-directed magnetic pinching force, and the smaller H is, the smaller the total pressure on a cylinder of radius r will be compared to the pressure on the rotation axis, owing to a larger dimensionless radius $x = r/H$. On the other hand, if $H \to \infty$, the flow will be isobaric. Therefore, the parameter H is crucial in determining the wind bubble shape. Also plotted in Figure 1 are the magnetic field strength (in units of $P_0^{1/2}$) and the ratio of the magnetic pressure to the gas pressure. The field strength peaks between $x = 1.0$ and 2.0, and the magnetic pressure is equal to the gas pressure at around $x = 2.0$.

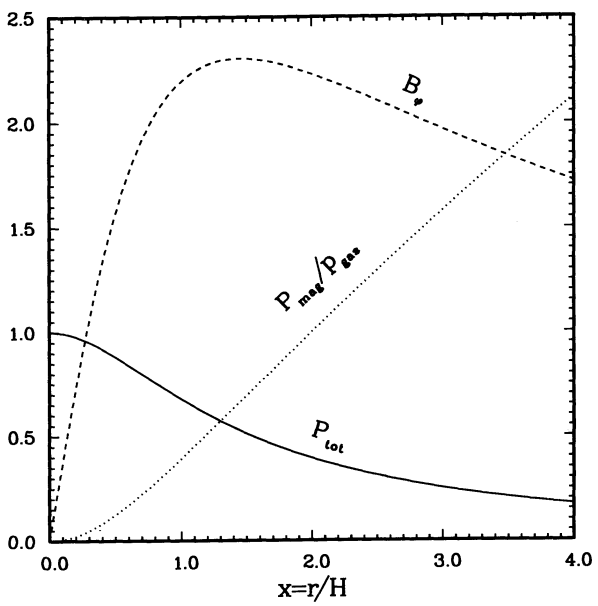

FIG. 1.—Radial structure of axisymmetric MHD model for pulsar wind bubble. The total pressure (in units of P_0, *solid line*), magnetic field strength (in units of $P_0^{1/2}$, *dashed line*), and ratio of magnetic presssure to gas pressure (*dotted line*) are plotted against the scaled cylindrical radius $x = r/H$.

3. GROWTH AND ELONGATION OF CRAB PULSAR WIND BUBBLE

In this section, we demonstrate that the pressure difference across the Crab pulsar wind bubble can be responsible for its present-day elongation. We associate the wind bubble with the inner region of Velusamy's (1985) 20 cm radio map of the Crab nebula (his Fig. 1*a*), which is also the region within which most of the optical continuum is emitted (Woltjer 1957; Fesen & Blair 1990). If the wind bubble's major axis were in the plane of sky, then for a distance of 2 kpc to the Crab, the size of this region would be about 3.2 × 2.0 pc, which is significantly smaller than that of the outermost radio and optical line-emitting filament structure (4.4 × 3.2 pc: Gull & Fesen 1982; Veulusamy 1985). Indirect support for this association comes from the existence of the two dark "bays" on optical continuum plates (Fesen & Blair 1991; Fesen et al. 1992), which could be interpreted as portions of the shell that marks the boundary of the relativistic fluid in the wind bubble (Li & Begelman 1992a).

The present-day shape of the wind bubble is a cumulative result of its evolution, which is controlled by the outward pressure force on its expanding shell on the one hand and the density distribution of the ambient medium on the other. The quasi-static solutions developed in § 2 should be applicable in determining the pressure inside the wind bubble throughout most of its evolution. This is because, given the present size of the wind bubble, it must have spent most of its time expanding more slowly than about 2000 km s^{-1}, i.e., much slower than the fast magnetosonic speed in its interior. To model the ambient medium, we shall follow Chevalier (1984) and consider three separate cases: a uniform interstellar medium; a slow progenitor stellar wind with density inversely proportional to the square of the radius; and fast-moving uniform supernova ejecta, the density of which decreases with time as t^{-3}.

In the "thin shell" approximation (Mac Low & McCray 1987), the governing equations for the evolution of the pulsar wind bubble are the same as those given in Li & Begelman (1992a, eqs. [2]–[5]), except that the magnetic contributions to the energy and pressure must be included. For simplicity, we shall assume that the pulsar power output L and the scale length H are time-independent. To obtain dimensionless forms of the equations, we can express the scales for length, speed, and pressure in terms of scale time $T = 938$ yr, density D, and power output L as $R = (LT^3/D)^{1/5}$, $V = [L/(T^2D)]^{1/5}$, and $P = (L^2D^3/T^4)^{1/5}$.

We solve the governing equations numerically. As a check, our programs recover the analytic solutions in the absence of a magnetic field, i.e., when $H = \infty$. For each type of ambient medium, the dimensionless parameter h ($= H/R$) is fixed by requiring that the ratio of the computed wind bubble length to its width be 1.6 (= 3.2 pc/2.0 pc) at the present time (the scaled time $t = 1$). The length scale R is obtained by setting the width of the wind bubble to be 2.0 pc. The required ratio of L/D

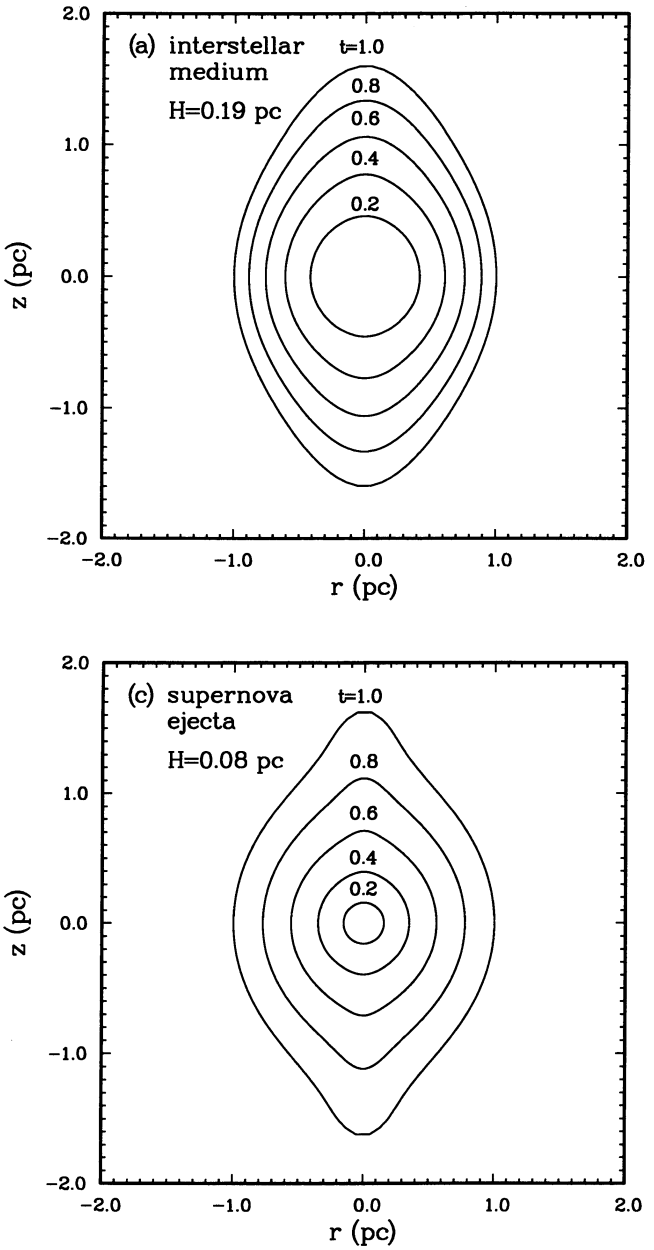

FIG. 2.—Time evolution of the pulsar wind bubble inside three different ambient media: (*a*) uniform interstellar medium (*b*) slow progenitor stellar wind, and (*c*) fast-moving SN ejecta. The different contours are the wind bubble's shapes and sizes at scaled times $t = 0.2$, 0.4, 0.6, 0.8, and 1.0, and all contours are rescaled so that the outermost ones have widths of 2 pc.

follows immediately from the definition of R. We plot the evolution of the pulsar wind bubble in Figure 2. In Table 1, we list H and the ratio of the pulsar output to the ambient density for each type of ambient medium, together with the corresponding present-day values for P_0 and the free pulsar wind magnetization parameter σ. Given P_0 and H, σ is estimated as follows: by balancing the thrust in the pulsar wind against the pressure in the wind bubble, we estimate a radius $r_s \cong [L/(6\pi P_0 c)]^{1/2}$ for the wind-terminating shock (KC1), which is much smaller than H. From the Rankine-Hugoniot shock jump conditions (KC1) for a transverse MHD shock, one can express σ in terms of downsteam quantities as $\sigma = B^2/(54\pi P^2)$. From equation (11b), one has $B^2 \propto r_s^2$ for $x_s \equiv r_s/H \ll 1$. Substituting for r_s, we finally have

$$\sigma \cong \frac{L}{72\pi P_0 H^2 c} . \tag{12}$$

As is evident from Table 1, the value of σ thus obtained is indeed small in each case and is consistent with the earlier results of spherical models, which range from 1.6×10^{-3} (Emmering & Chevalier 1987) to about 10^{-2} (Rees & Gunn 1974). Our estimates are very close to the best value obtained by KC1, 3×10^{-3}. In other words, *the value of σ inferred from independent arguments is just enough to elongate the Crab Nebula to the observed degree.*

We shall henceforth restrict our discussion to the case of a slow progenitor stellar wind. This choice is motivated by our models for the evolution of the two dark "bays" in the synchrotron nebula (Li & Begelman 1992a). We find that the bays can be produced by the advance of the wind bubble into a slow progenitor wind possessing a mild density stratification normal to the plane bisecting the bays. To produce similar structures in the interstellar medium would require an implausibly high ambient density, given the Crab Nebula's location about 200 pc below the Galactic plane, and even then the current separation speed of the bays would be slower than

TABLE 1

PROPERTIES OF THE MAGNETIZED PULSAR WIND BUBBLE INSIDE THREE DIFFERENT TYPES OF AMBIENT MEDIA

Type of Medium	H (pc)	L_0/ρ[a]	P_0[b]	σ
Interstellar medium	0.19	0.49	8.56	2.52×10^{-3}
Slow progenitor wind	0.26	1.70	4.71	2.44×10^{-3}
Fast supernova ejecta	0.08	0.24	19.6	5.91×10^{-3}

[a] L_0 is the pulsar power output L in units of 5×10^{38} ergs s^{-1}, and the ambient density ρ is in units of 2.3×10^{-24} g cm^{-3}. In the case of slow progenitor wind, ρ refers to the wind density at 1 pc.

[b] The pressure P_0 is in units of $10^{-8} L_0$ dyn cm^{-2}.

observed (Fesen et al. 1992). To produce bays in fast-moving ejecta, the density stratification would have to be unreasonably large.

We reiterate that the above calculations were carried out under the assumption that H is time-independent. According to equation (12), this would imply that σ had to be smaller in the past due to a higher P_0. If, on the other hand, σ is assumed to be time-independent, then H would increase with time. We have recomputed the wind bubble evolution for the case of slow progenitor wind, holding σ constant. We find that $\sigma = 6.6 \times 10^{-4}$, and the present values for H and P_0 are 0.82 pc and $1.75 \times 10^{-8}\ L_0$ dyn cm^{-2}, respectively, where L_0 is the pulsar power output L in units of 5×10^{38} ergs s^{-1}. As expected, H is larger than that listed in Table 1, whereas σ is smaller.

If the pulsar rotation axis is tilted into the plane of sky by an angle of 30°, as was suggested by Pelling et al. (1987), then we have underestimated the length of the wind bubble by a factor of $(\cos 30°)^{-1} = 1.155$. In this case, further magnetic pinching is needed compared to the untilted case. For the slow progenitor wind, if we hold H constant throughout the evolution of the wind bubble, we have $H = 0.22$ pc, $P_0 = 5.2 \times 10^{-8}\ L_0$ dyn cm^{-2}, and $\sigma = 3.4 \times 10^{-3}$; if, on the other hand, we hold σ constant, then we have $\sigma = 9.6 \times 10^{-4}$, $H = 0.73$ pc, and $P_0 = 1.5 \times 10^{-8}\ L_0$ dyn cm^{-2}. In both cases, the values for σ are somewhat larger than those in the corresponding untilted cases but are still not much different from the values obtained in spherical models.

4. COMPARATIVE MORPHOLOGY OF THE OPTICAL AND X-RAY SYNCHROTRON NEBULAE

To determine the morphology of the synchrotron nebula observed at a given wavelength, one needs to know not only the magnetic field structure and the velocity field inside the pulsar wind bubble, but also the synchrotron particle distribution function injected into the wind bubble. In this section, we shall reverse the problem and use the observed sizes of the synchrotron nebulae at optical and X-ray wavelengths, together with the inferred magnetic field structure from last-section, to constrain the particle injection function. Since the velocity field inside the pulsar wind bubble cannot be determined uniquely in our quasi-static treatment (§ 2.2.), we shall adopt the simplest case of a radial flow pattern. The flow field is then fixed by the conservation of mass flux along each streamline, together with the flow boundary condition at the edge of the wind bubble, which we take to be an ellipsoid of 3.2×2.0 pc. For simplicity, we assume that the flow speed at each point on the ellipsoid is proportional to its distance from the origin and has a largest value along the major axis of 2000 km s^{-1}. For this reason, our discussion will be restricted only to the overall dimensions of the nebulae, and we shall not attempt to address more detailed properties of the surface brightness distribution.

The formulation of the problem is analogous to that of Kennel & Coroniti (KC2) for computing radiation from a spherical pulsar wind bubble, except that the problem in our case is axisymmetric. We present the derivation of the synchrotron spectral emissivity j_ν inside the wind bubble in the Appendix. An important feature that is apparent from equation (A10) is that j_ν depends strongly on the cylindrical radius via $[P(r)]^{(2\alpha+3)/4}[B(r)]^{\alpha+1}$. This strong r-dependence is the basic reason that the computed nebular shapes for optical and longer wavelengths, where the synchrotron "burn-off effect" is not severe, tend to be elongated along the axis. At shorter wavelengths such as X-rays, the condition $c_{\min} > 1$ (where j_ν vanishes, see eq. [A9]) is satisfied more readily, and the nebular shapes depend more on the details of the particle distribution function.

To obtain surface brightness, one has only to integrate j_ν along the line of sight. In each panel of Figure 3, we show surface brightness contours, at 0.1% and 50% of the maximum brightness, for three representative energies: 2 eV (optical), 2.5 keV (soft X-ray [Harnden & Seward 1984]), and 40 keV (hard X-ray [Pelling et al. 1987]). The panels illustrate the effects of different particle injection functions. We find that streamline-independent particle injection at the origin always gives rise to contours which are much too elongated along the axis to be compatible with those observed, as exemplified by Figure 3*a*. Although we have tried several different streamline configurations, the results remain qualitatively the same, and primarily reflect the basic field structure inside the wind bubble.

The nebulae observed in soft X-rays (Harnden & Seward 1984) and hard X-rays (Pelling et al. 1987), however, are elongated along the equator. This motivates us to try injection functions with a lower maximum cutoff energy $\epsilon^0_{\max}$ in the polar region, so as to concentrate the high-energy X-ray radiation in the equatorial region. Under this circumstance, the X-ray–emitting regions would be confined to tori, similar to those proposed by Aschenbach & Brinkmann (1975). Plotted in Figure 4 are the cross sections for these tori, in the case that $\epsilon^0_{\max}$ at the pole is lower by a factor of 20 compared to its value at the equator. The corresponding brightness contours with the same minimum energy $\epsilon^0_{\min}$ as in Figure 3*a* are shown in Figure 3*b*. The nebular shapes at X-ray wavelengths, as outlined by the 0.1% contours, resemble more closely the observed ones (Harnden & Seward 1984; Pelling et al. 1987) than do those in Figure 3*a*; however, the 50% contours still seem to be too elongated in all cases. These 50% contours can be brought into closer agreement with those observed by lowering the value of $\epsilon^0_{\min}$ in the polar region as well. The reason is that, by reducing $\epsilon^0_{\min}$, one effectively requires a larger particle number density n^0 (cf. eq. [A3]), and thus decreases the emissivity j_ν in the polar region (cf. eq. [A10] with $\alpha > 0.5$) with respect to that in the equatorial region. As an example, we plot in Figure 3*c* the contours with the same parameters as Figure 3*b*, except that $\epsilon^0_{\min}$ is lowered by a factor of 5 at the pole, for $\alpha = 0.75$. A higher (lower) contrast is needed if α is smaller (larger).

Although we have assumed a radial geometry for the streamline configuration in the wind bubble, and Figures 3 and 4 are meant to be illustrative, a general conclusion can still be drawn about the particle injection function: the injection function cannot be isotropic, with the same $\epsilon^0_{\max}$ and $\epsilon^0_{\min}$ on all streamlines. Instead, the maximum cutoff energy has to be much higher in the equatorial region than in the polar region in order for the overall morphologies of the model X-ray nebular to be comparable to those observed. Better fits to the 50% contours are obtained if the minimum cutoff energy is also larger near the equator. The exact streamline dependence of the particle distribution function, however, cannot be determined without treating the velocity field self-consistently. Since $\epsilon^0_{\min}$ is directly proportional to the Lorentz factor γ in the free pulsar wind in the limit of small σ and for a transverse shock (KC1), a larger $\epsilon^0_{\min}$ near the equator would imply that the free wind moves faster there. How the distribution of $\epsilon^0_{\max}$ is related to the pulsar wind properties is not clear at present.

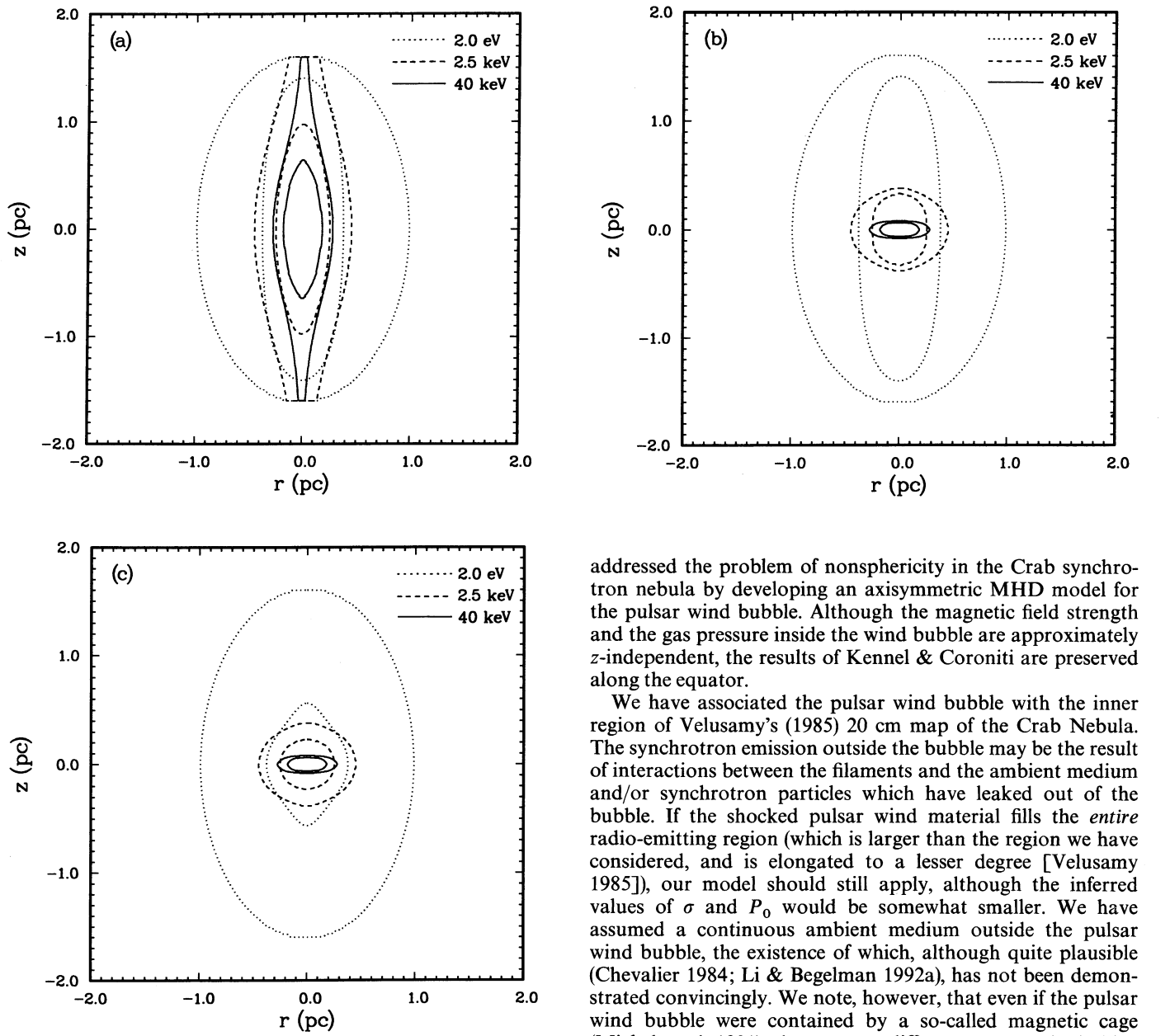

FIG. 3.—Contours of 0.1% and 50% of the peak surface brightness for synchrotron radiation at optical (2 eV, *dotted lines*), soft X-ray (2.5 keV, *dashed lines*), and hard X-ray (40 keV, *solid lines*) energies, from a pulsar wind bubble with $H = 0.5$ pc and $P_0 = 3 \times 10^{-8}$ dyn cm^{-2}. The particle injection function (eq. [A1]) is assumed to be a power law between maximum energy ϵ^0_{max} and minimum energy ϵ^0_{min}, with $\alpha = 0.75$. (*a*) Contours for a uniform injection function with $\epsilon^0_{max} = 10^9$ and $\epsilon^0_{min} = 10^5$; (*b*) ϵ^0_{min} remains the same as in (*a*), but ϵ^0_{max} is reduced by a factor of 20 toward the pole according to $\epsilon^0_{max} = [0.05 + 0.95 \exp(-\theta/\theta_0)] \times 10^9$, where θ is the polar angle from the pulsar equator, and the high-energy particles are concentrated within an angle $\theta_0 = 12°$ around the equator; and (*c*) ϵ^0_{max} is the same as in (*b*), whereas ϵ^0_{min} is reduced by a factor of 5 toward the pole according to $\epsilon^0_{min} = [(0.2 + 0.8 \exp(-\theta^2/\theta_0^2)] \times 10^5$, where $\theta_0 = 30°$.

5. DISCUSSION

The great successes of the earlier spherical MHD models for the Crab Nebula (Rees & Gunn 1974; KC1; KC2) have motivated us to develop them further. In this paper, we have mainly addressed the problem of nonsphericity in the Crab synchrotron nebula by developing an axisymmetric MHD model for the pulsar wind bubble. Although the magnetic field strength and the gas pressure inside the wind bubble are approximately z-independent, the results of Kennel & Coroniti are preserved along the equator.

We have associated the pulsar wind bubble with the inner region of Velusamy's (1985) 20 cm map of the Crab Nebula. The synchrotron emission outside the bubble may be the result of interactions between the filaments and the ambient medium and/or synchrotron particles which have leaked out of the bubble. If the shocked pulsar wind material fills the *entire* radio-emitting region (which is larger than the region we have considered, and is elongated to a lesser degree [Velusamy 1985]), our model should still apply, although the inferred values of σ and P_0 would be somewhat smaller. We have assumed a continuous ambient medium outside the pulsar wind bubble, the existence of which, although quite plausible (Chevalier 1984; Li & Begelman 1992a), has not been demonstrated convincingly. We note, however, that even if the pulsar wind bubble were contained by a so-called magnetic cage (Michel et al. 1991), the pressure difference across the bubble (due to the magnetic pinching) would still elongate the "cage" and thus the synchrotron nebula inside, although the degree of elongation would be difficult to evaluate quantitatively.

The fraction of the spindown power output of the Crab pulsar that goes into the internal energy of the wind bubble fluid and adiabatic expansion against the ambient medium (L) is uncertain (Li & Begelman 1992a). Although L does not affect the shape of the wind bubble (and thus σ), it does control the pressure ($\propto L$; see Table 1) and the magnetic field strength ($\propto L^{1/2}$) inside the bubble. For the case of a slow progenitor stellar wind as the ambient medium, a magnetic field strength of 4×10^{-4} G inside the bubble (Swanbank 1980) implies $L \cong 5 \times 10^{38}$ ergs s^{-1}.

Our model does not apply to regions where the magnetic field is predominantly poloidal, as seems to be the case near the eastern "bay" (Hickson & van den Bergh 1991). If the eastern and western "bays" are physically connected and are portions

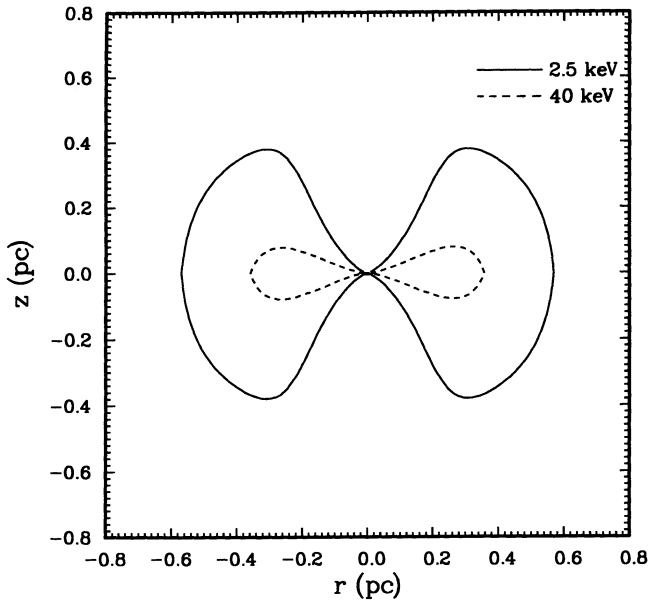

FIG. 4.—Cross sections of the 2.5 keV (*solid*) and 40 keV (*dashed*) X-ray–emitting tori for the distribution of ϵ^0_{max} assumed in Figs. 3*b* and 3*c*. The spectral emissivity j_ν is negligible outside the solid (*dashed*) line for 2.5 (40) keV X-rays.

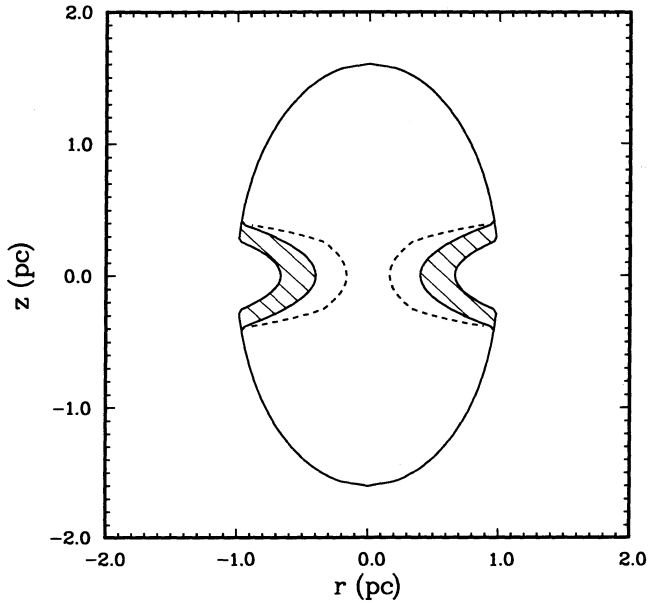

FIG. 5.—Magnetic field geometry used to illustrate possible explanation for "hourglass" morphology in total polarized light (Michel et al. 1991). The indentations in the boundary of the nebula represent the "bays," which in reality are misaligned with respect to the pulsar's equatorial plane. The magnetic field inside volume whose cross section is the shaded region is parallel to the pulsar rotation axis; field is toroidal elsewhere in bubble. The dashed lines are the places where there is no totally polarized light, due to superposition of the two orthogonal polarized components. We have assumed a uniform field strength and uniform power-law particle energy distribution function with $\alpha = 0.75$.

of a torus enclosing the remnant's center of explosion (Fesen et al. 1992), then the interaction of the bubble with this torus could induce a transition of the magnetic field from predominantly toroidal close to the pulsar to the nearly poloidal around the "bays," since the torus's normal is misaligned with the rotation axis of the pulsar. It is interesting to notice in this connection that a region of poloidal field near the torus superposed on top of a region of toroidal field near the pulsar could explain the "hourglass" shape of the total polarized optical light obtained by Michel et al. (1991). This is demonstrated with the simple magnetic field configuration shown in Figure 5, where the field is parallel to the axis in a volume whose cross section is the shaded region and is toroidal elsewhere. We assume a uniform power-law particle distribution and constant field strength everywhere. The contours of zero polarization, which correspond to the darkest zones in Plate 8 of Michel et al. (showing the total polarized light), are also plotted in Figure 5. We believe that the "X"-type morphology of the null polarization zone, where the polarized light from regions of different magnetic field orientations cancel one another, makes the total polarized light appear to have an "hourglass" morphology.

We have not addressed the origin of the low σ in the free Crab pulsar wind. In a magnetically stripped wind model, Coroniti (1990) proposed that annihilation of toroidal field of opposite polarity can convert the high σ wind expected near the Crab pulsar to the low-σ wind required upstream of the wind-terminating shock, provided that the magnetic dipole is inclined by about 80° to the pulsar's rotation axis. Alternatively, a low-σ wind can be achieved via the so-called magnetic nozzle effect if the flux tubes diverge more rapidly than those in a radial wind (Camenzind 1989; Li & Begelman, 1992b). A further complication arises in the equatorial region where the nebular toroidal fields reverse their directions across the equatorial plane (Rees & Gunn 1974), and reconnection is expected to occur. In the reconnection region, our quasi-static treatment breaks down, but we do not expect this region to affect the overall structure of nebular magnetic field much. The potentially important question of how the reconnection affects the synchrotron particle injection function is not attempted in this paper and will be addressed in future works.

To summarize, we have extended Kennel & Coroniti's spherical MHD models of the Crab Nebula in two significant ways. First, we have demonstrated that the pinching effect of the toroidal field is dynamically important and can explain the overall shape of the Crab pulsar wind bubble. Second, we have used the inferred magnetic field structure inside the pulsar wind bubble to show that sizes and shapes of the X-ray nebulae can be understood if the high-energy X-ray–emitting particles are injected preferentially in the equatorial region of the Crab pulsar.

This research was supported in part by NSF grant AST88–16140 and NASA Astrophysical Theory Center grant NAGW-766.

APPENDIX

DERIVATION OF THE SYNCHROTRON SPECTRAL EMISSIVITY j_ν

Throughout this derivation, a curvilinear coordinate system (ψ, s) is used, with s measuring the distance from the origin along a streamline ψ. Synchrotron particles are injected at the shock front $s = s^0(\psi)$, where the free pulsar wind is terminated, with a

power-law energy distribution

$$f^0(\epsilon^0, \psi) = \frac{D(\psi)}{4\pi} (\epsilon^0)^{-(2\alpha+1)} \tag{A1}$$

between $\epsilon^0_{\rm min}(\psi)$ and $\epsilon^0_{\rm max}(\psi)$ (where $\epsilon \equiv E/mc^2$). The superscript "0" denotes a quantity evaluated at the shock front. In the limit that $\epsilon^0_{\rm max} \gg \epsilon^0_{\rm min}$, the normalization factor $D(\psi)$ becomes

$$D \cong 2\alpha n^0 [\epsilon^0_{\rm min}]^{2\alpha} \cong 2\alpha \left[\frac{3}{2}\frac{2\alpha-1}{2\alpha}\frac{P_0}{mc^2}\right]^{2\alpha} (n^0)^{1-2\alpha} \tag{A2}$$

where $n^0(\psi)$ is the particle number density and the spectral index α is taken to be streamline-independent constant between 0.5 and 1. The last step in equation (A2) follows from the Rankine-Hugoniot relation (KC2, eq. [2.6a]):

$$\epsilon^0_{\rm min} = \frac{3}{2}\left(\frac{2\alpha-1}{2\alpha}\right)\frac{P_0}{n^0 mc^2} . \tag{A3}$$

The evolution of a particle's energy $\epsilon(\psi, s)$ along a streamline ψ, averaged over an isotropic distribution of pitch angles, is governed by

$$\frac{d\epsilon}{dt} = \epsilon \frac{d\ln n^{1/3}}{dt} - \frac{4e^4}{9m^3c^5} B(r)^2\epsilon^2 \tag{A4}$$

which can be integrated once to obtain

$$\epsilon = \left[\frac{(n^0)^{1/3}}{n^{1/3}\epsilon^0} + \frac{1}{\epsilon_\infty}\right]^{-1} , \tag{A5a}$$

where

$$\epsilon_\infty \equiv n^{1/3}\left[\frac{4}{9}\frac{e^4}{m^3c^5}\int_{s0}^{s}\frac{B(r)^2 n^{1/3}}{v}\,ds\right]^{-1} \tag{A5b}$$

is the maximum possible energy at location (ψ, s), and $v = ds/dt$ has been used.

From the conservation of the particle number and equation (A5), we can obtain the particle distribution function $f(\epsilon, \psi, s)$ anywhere inside the wind bubble:

$$f = \frac{K}{4\pi}\left(\frac{n}{n^0}\right)^{(2\alpha/3)+1}\frac{n^0}{\epsilon^2}\left(\frac{1}{\epsilon}-\frac{1}{\epsilon_\infty}\right)^{2\alpha-1} , \tag{A6}$$

where K is a constant which depends only on α. Notice that there is an error in KC2's equation (2.14), where the exponent for $(1/\epsilon - 1/\epsilon_\infty)$ should be $2\alpha - 1$, as in equation (A6), instead of $2\alpha - 3$. The spectral power emitted by a particle of energy ϵ and pitch angle θ_p into a unit solid angle around polar angle θ to the local magnetic field, $P_\nu(\epsilon, \theta_p, \theta)$, can be computed as follows. Since the synchrotron radiation is concentrated on a cone of half-angle θ_p around the magnetic field direction and the emitted spectrum is peaked around characteristic frequency ν_c (Rybicki & Lightman 1979), one can roughly approximate $P_\nu(\epsilon, \theta_p, \theta)$ by the following two δ-functions:

$$P_\nu \cong \frac{2e^4B^2\epsilon^2}{3m^2c^3}\sin^2\theta_p\,\delta(\nu-\nu_c)\frac{\delta\cos\theta_p - \cos\theta}{2\pi} , \tag{A7}$$

where $\nu_c = 3f_c\epsilon^2\sin\theta_p/2$ and $f_c \equiv eB/(2\pi mc)$. Summing up contributions from particles of all energies and pitch angles at location (ψ, s), we arrive at the spectral emissivity

$$j_\nu(\psi, s, \theta) = 4\pi\int_0^1 d\cos\theta_p\int_{\epsilon_{\rm min}}^{\epsilon_{\rm max}} d\epsilon f(\epsilon, \psi, s)P_\nu(\epsilon, \theta_p, \theta) , \tag{A8}$$

where $\epsilon_{\rm min}$ and $\epsilon_{\rm max}$ are the local minimum and maximum particle energies and are obtained by substituting $\epsilon^0_{\rm min}$ and $\epsilon^0_{\rm max}$ for ϵ^0 in equation (A5a). Before integration of above equation, three auxiliary dimensionless quantities are defined:

$$c_{\rm min} \equiv \frac{2\nu}{3f_c(\epsilon_{\rm max})^2} , \qquad c_{\rm max} \equiv \frac{2\nu}{3f_c(\epsilon_{\rm min})^2} , \qquad c_\infty \equiv \frac{2\nu}{3f_c\epsilon_\infty^2} , \tag{A9}$$

where $c_\infty \le c_{\rm min} \le c_{\rm max}$. Carrying out the double integrations in equation (A8), we find that, if $\sin\theta \in (c_{\rm min}, c_{\rm max})$, one has

$$\nu j_\nu = \frac{\alpha}{6\pi}\frac{e^4}{m^2c^3}\left(\frac{3}{2}\frac{2\alpha-1}{2\alpha}\frac{1}{mc^2}\right)^{2\alpha}\left(\frac{3f_c}{2\nu}\right)^{\alpha-1} P_0^{(6\alpha-3)/4}P(r)^{(2\alpha+3)/4}B(r)^2(\sin\theta)^{1+\alpha}\left[\left(1-\sqrt{\frac{c_\infty}{\sin\theta}}\right)\Big/ n^0\right]^{2\alpha-1} , \tag{A10}$$

and the integral is equal to zero otherwise. We have used equation (A2) in deriving the above equation. Apparently, when $c_{\rm min} \ge 1$, no radiation of frequency ν can be emitted at this location and beyond along the same streamline. This is, of course, a manifestation

of the so-called synchrotron burn-off effect. (A more exact expression for eq. [A7] would, of course, yield an exponential cutoff rather than a step function.)

For illustrative purposes, we choose the simplest possible streamline configuration—radial flow. The stream function ψ can then be replaced by the polar angle Θ measured from the rotation axis and s is now equivalent to $r/\sin\Theta$. Since the free pulsar wind occupies only a small fraction of the Crab Nebula volume, we can further assume that $s^0 = 0$ for simplicity.

REFERENCES

Arons, J. 1991, in IAU Colloq. 128, Magnetospheric Structure and Emission Mechanisms of Radio Pulsars, ed. J. A. Gil, T. H. Hankins, & J. M. Rankin, in press
Aschenbach, B., & Brinkmann, W. 1975, A&A, 41, 147
Camenzind, M. 1989, in Accretion Disks and Magnetic Fields in Astrophysics, ed. G. Belvedere (Dordrecht: Kluwer), 129
Chevalier, R. A. 1984, ApJ, 280, 797
Coroniti, F. V. 1990, ApJ, 349, 538
Emmering, R. T., & Chevalier, R. A. 1987, ApJ, 321, 334
Fesen, R. A., & Blair, W. P. 1990, ApJ, 351, L45
Fesen, R. A., Martin, C., & Shull, J. M. 1992, ApJ, in press
Gull, T. R., & Fesen, R. A. 1982, ApJ, 260, L75
Harnden, F. R., Jr., & Seward, F. D. 1984, ApJ, 283, 279
Hickson, P., & van den Bergh, S. 1990, ApJ, 365, 224
Kennel, C. F., & Coroniti, F. V. 1984a, ApJ, 283, 694 (KC1)
———. 1984b, ApJ, 283, 710 (KC2)
Li, Z.-Y., & Begelman, M. C. 1992a, ApJ, in press
———. 1992b, in preparation
Mac Low, M. M., & McCray, R. 1987, ApJ, 320, 776
Michel, F. C. 1982, Rev. Mod. Phys., 54, 1
Michel, F. C., Scowen, P. A., Dufour, R. J., & Hester, J. J. 1991, ApJ, 368, 463
Pelling, R. M., Paciesas, W. S., Peterson, L. E., Makishima, K., Oda, M., Ogawara, Y., & Miyamoto, S. 1987, ApJ, 319, 416
Rees, M. J., & Gunn, J. E. 1974, MNRAS, 167, 1
Rybicki, G. B., & Lightman, A. P. 1979, Radiative Processes in Astrophysics (New York: Wiley)
Schmidt, G. R., Angel, J. R. P., & Beaver, E. A. 1979, ApJ, 227, 106
Swanbank, E. 1980, MNRAS, 193, 451
Trimble, V. 1985, in The Crab Nebula and Related Supernova Remnants, ed. M. C. Kafatos & R. B. C. Henry (Cambridge: Cambridge Univ. Press), 257
Velusamy, T. 1985, MNRAS, 212, 359
Woltjer, L. 1957, BAN, 13, 301